communications chemistry

A Nature Portfolio journal

Article

https://doi.org/10.1038/s42004-026-01941-8

ABEL-FRET bridges the timescale gap in single-molecule measurements of the structural dynamics in the A_{2A} adenosine receptor

Ivan Maslov[1,2,3], Valentin Borshchevskiy[4], Iván Pérez[5], Vadim Cherezov[6], Johan Hofkens[2,7], Jelle Hendrix[1], Michael Börsch[5] ✉ & Thomas Gensch[8] ✉

The functional complexity of G protein-coupled receptors (GPCRs) arises from their structural dynamics, spanning timescales from nanoseconds to minutes. Single-molecule Förster Resonance Energy Transfer (smFRET) enables direct observation of these dynamics in individual receptors, either freely diffusing in solution, using confocal microscopy, or immobilized on surfaces, using Total Internal Reflection Fluorescence (TIRF) camera-based microscopy. However, these modalities are limited to distinct timescales – faster than milliseconds or slower than hundreds of milliseconds, respectively. To overcome these limitations, we employed smFRET with Anti-Brownian Electrokinetic (ABEL) trapping to extend the observation time of untethered human A_{2A} adenosine receptors (A_{2A}AR) reconstituted in lipid nanodiscs from milliseconds to seconds. We characterized conformational heterogeneity in apo and ligand-bound A_{2A}AR and updated previous estimates of dwell times for long-lived receptor states from milliseconds to hundreds of milliseconds. Our results highlight the power of ABEL-FRET to probe GPCRs dynamics and offer valuable insights into GPCR conformational landscapes.

G protein-coupled receptors (GPCRs) orchestrate critical physiological processes such as vision, neurotransmission, inflammation, and blood pressure regulation. Characterized by their seven-transmembrane helix topology, GPCRs constitute the largest family of membrane proteins in the human genome, encompassing over 800 members[1,2]. Their central role in human health is underscored by the fact that more than 30% of all FDA-approved drugs target GPCRs as their primary mode of action[3,4]. Many endogenous ligands and drugs bind to the extracellular ligand-binding pockets of GPCRs, triggering conformational changes in the transmembrane and intracellular regions, which alter interactions between the receptors and their intracellular signaling partners, such as G proteins and arrestins[5,6]. The structural flexibility of GPCRs underlies the wide variety of mechanisms by which ligands modulate the receptors' activity[7–9]. For example, a GPCR can exhibit various activity levels when bound to agonists with different efficacies[10]. The activity of an agonist-bound GPCR can be further tuned by allosteric modulators that bind to additional, less evolutionary conserved pockets in the receptor's structure[11,12]. Finally, biased agonists shift the equilibrium between various signaling pathways triggered by the same GPCR (e.g., those mediated via various types of G proteins, arrestins, or GRK kinases)[13,14]. This diversity in the pharmacological profiles of GPCR ligands opens opportunities for more effective use of GPCR-targeted drugs in clinical settings. However, the structural flexibility of GPCRs, which underlies their complex pharmacology, poses serious challenges for structure-based drug design and for the understanding of fundamental mechanisms of GPCR activation.

Despite the challenges posed by the structural flexibility of GPCRs in obtaining high-resolution structures via X-ray crystallography or cryo-electron microscopy, these techniques have significantly advanced our understanding of the structure-function relationship in GPCRs[15,16]. A notable drawback of these techniques is that they provide only static

[1]Dynamic Bioimaging Lab, Advanced Optical Microscopy Centre and Biomedical Research Institute (BIOMED), Hasselt University, Diepenbeek, Belgium. [2]Department of Chemistry, KU Leuven, Leuven, Belgium. [3]Department of Biochemistry, Groningen Biomolecular Sciences and Biotechnology Institute, University of Groningen, Groningen, The Netherlands. [4]Institute of Biological Information Processing 7, IBI-7 (Structural Biochemistry), Forschungszentrum Jülich, Jülich, Germany. [5]Jena University Hospital, Single Molecule Microscopy Group, Jena, Germany. [6]Bridge Institute, Department of Chemistry, University of Southern California, Los Angeles, CA, USA. [7]Department of Molecular Spectroscopy, Max Planck Institute for Polymer Research, Mainz, Germany. [8]Institute of Biological Information Processing, Molecular and Cellular Physiology (IBI-1), Forschungszentrum Jülich GmbH, Jülich, Germany. ✉e-mail: michael.boersch@med.uni-jena.de; t.gensch@fz-juelich.de

snapshots of stable conformational states, with limited information about conformational dynamics[8]. A diverse set of complementary methods, including nuclear magnetic resonance (NMR), double electron-electron resonance (DEER), mass-spectrometry, and single-molecule fluorescence microscopy, reveals structural heterogeneity and complex conformational dynamics in GPCRs[8,17]. They show that receptors switch between multiple stable states on timescales ranging from nanoseconds to seconds[8,17]. Faster motions correspond to near-equilibrium vibrations and rotations of amino acid side chains and unstructured parts of the receptor, while slower motions involve higher-order rearrangements of secondary structure elements and loops[7]. GPCR ligands, ranging from inverse to full agonists and including biased agonists and allosteric modulators, affect the rates of conformational changes in GPCRs and the relative populations of stable conformations[18].

Single-molecule fluorescence microscopy is a powerful method for monitoring conformational dynamics in proteins and, in particular, GPCRs[19,20]. Single-molecule sensitivity of fluorescence microscopy surpasses the need for ensemble averaging, allowing the identification of distinct protein states that co-exist within an ensemble of proteins under equilibrium conditions. Conformational changes in a protein are typically monitored based on conformation-dependent fluorescence changes from a single environment-sensitive fluorescent dye (e.g., in single-molecule photoisomerization-related fluorescence enhancement (smPIFE[21]), photoinduced electron transfer (PET[22])) or a pair of donor and acceptor dyes for single-molecule Förster resonance energy transfer (smFRET)[23,24]. In smFRET experiments, the conformational changes of the protein affect the proximity and relative orientations of the fluorophores attached to its mobile structural elements, leading to changes in the efficiency of energy transfer from the donor to the acceptor dye (Fig. 1a). FRET is extremely sensitive to variations in the mutual position of the dyes, including inter-dye distance changes at the Ångström-scale and alterations of the dye orientations, which result in measurable changes of the ratio between donor and acceptor fluorescence intensities, making this technique highly sensitive for observing conformational dynamics.

SmFRET experiments are typically performed in one of two modalities, depending on whether proteins freely diffuse in the sample or are immobilized on a glass surface[24]. In the first modality, freely diffusing molecules transiently cross the detection volume of a confocal fluorescence microscope. The observation time is defined by the diffusion of the molecule under investigation across the detection volume, which typically occurs within one to a few milliseconds. In the second modality, target molecules are immobilized on a cover glass and imaged via a TIRF microscope or a scanning confocal microscope, allowing observation of slower conformational dynamics[25]. Immobilized molecules can be observed for longer periods, up to several minutes or even hours, limited mostly by photobleaching of the fluorescent dyes[26–28]. Immobilization of target molecules by tethering and their interaction with the surface, however, can potentially affect their structural dynamics, posing challenges for immobilization-based experiments[24,29,30]. Alternative approaches to observing individual fluorescently labeled molecules for longer periods without immobilization include measuring diffusion in viscous media, e.g., glycerol, or a polyacrylamide gel[31–33], conjugating molecules to large slowly-diffusing particles or liposomes[34], confining freely diffusing molecules within a microfluidic chip[35,36], or tracking them, e.g., via orbital tracking[37–39] or camera-based tracking within excitation region of highly inclined and laminated optical (HiLO) excitation[31]. The diffusion of fluorescently labeled molecules in solution can also be actively counteracted using an Anti-Brownian ELectrokinetic (ABEL) trap, where untethered molecules are held in the field of view of a microscope for up to several minutes, enabling the monitoring of slow conformational dynamics, all while molecules are not physically tethered[40–44].

In an ABEL trap, molecules diffuse within a ~1-micron-thin plane of a microfluidic device and transiently enter the detection area of a scanning confocal microscope (Fig. 1b). When a fluorescently labeled molecule enters this region, its position is estimated in real time based on its fluorescence emission. An external electric field—controlled by a feedback loop and applied via electrodes—is then used to counteract the molecule's random Brownian motion and to maintain it near the center of the scanned area[41]. By rapidly adjusting the applied voltages, charged molecules can be stably held within the microscope's field of view for durations ranging from seconds to minutes—several orders of magnitude longer than in traditional diffusion-limited single-molecule experiments. During this extended observation time, emitted photons are continuously recorded, enabling detailed analysis of the molecule's conformational dynamics. The resolution down to a single base pair in a dsDNA sample (0.34 nm) was demonstrated for ABEL-FRET[42,45]. ABEL trapping has previously been used to monitor monomer-dimer transitions of GPCRs extracted from membranes using styrene–maleic acid copolymers (SMALPs), as well as conformational changes in GPCR monomers reconstituted in detergent micelles, using single-fluorophore labeling strategies[46,47].

Here we combined ABEL trapping with smFRET to investigate the conformational dynamics of a prototypical GPCR, the human A_{2A} adenosine receptor (A_{2A}AR). A_{2A}AR plays an important role in the regulation of cardiovascular tonus, sleep, inflammation, and neurotransmission of dopamine and glutamate[48,49]. It is a promising target for drugs against insomnia, chronic pain, depression, Parkinson's disease, and cancer[49–51]. A_{2A}AR is one of the most studied GPCRs, with two single-particle cryo-EM structures (cryogenic-electron microscopy)[52,53], two micro-crystal electron diffraction structures[54,55], and over 75 X-ray crystallographic structures available for the antagonist-bound[52,56,57] or agonist-bound[58,59] receptors as well as for a ternary complex of the receptor with an agonist and an engineered G protein[53,60]. NMR studies uncovered the conformational dynamics of A_{2A}AR across a broad range of time scales from nanoseconds[61] to milliseconds[62–65], and seconds[64,66]. PET combined with fluorescence correlation spectroscopy (PET-FCS[67]) and smFRET[68] detected sub-millisecond conformational dynamics in freely diffusing A_{2A}AR, while single-dye measurements with immobilized A_{2A}AR revealed slow conformational changes over several seconds[69,70]. In this study, we observed individual A_{2A}AR molecules in lipid nanodiscs for up to 2 s without immobilization using ABEL trapping and monitored their conformational dynamics and ligand-induced conformational changes using smFRET.

Results

ABEL-FRET measurements reveal structural heterogeneity and agonist-induced conformational changes in A_{2A}AR

To observe conformational dynamics in A_{2A}AR using smFRET, we fluorescently labeled and purified the recombinant human A_{2A}AR (Fig. 1a). For fluorescent labeling, two cysteine mutations were introduced: L225C$^{6.27}$ on the intracellular side of the transmembrane helix 6 (TM6) and Q310C$^{8.65}$ on the intracellular C-terminal helix 8 (H8, superscripts denote Ballesteros-Weinstein residue numbering in class A GPCRs[71]). These cysteines were labeled with donor and acceptor fluorophores, Alexa488-maleimide and Atto643-maleimide as in our previous study, where we used the same labeling positions and fluorescent dyes to measure sub-millisecond conformational dynamics in A_{2A}AR using burst-wise smFRET with freely diffusing molecules[68]. The functional integrity and homogeneity of the fluorescently labeled A_{2A}AR reconstituted in lipid nanodiscs was confirmed by size-exclusion chromatography (SEC) and a thermal shift assay (TSA) (Supplementary Fig. 1). Previously, using the samples from the same expression batch, we demonstrated that the FRET efficiency in the double-labeled $A_{2A}AR_{L225C/Q310C}$ increased upon receptor activation by agonists[72]. We also showed that changes in the relative orientations of the dyes contribute to this agonist-induced increase in the FRET efficiency; therefore, we did not interpret different FRET values as changes in inter-dye distances[68].

Using an ABEL trap, we now observed individual A_{2A}AR molecules typically for 0.1-1 s in the detection area of $2.34 \times 2.34\ \mu m^2$, i.e., a roughly 100-fold longer residence time (Fig. 1b–k) than previously achieved with smFRET of freely diffusing A_{2A}AR molecules in solution. We excited the

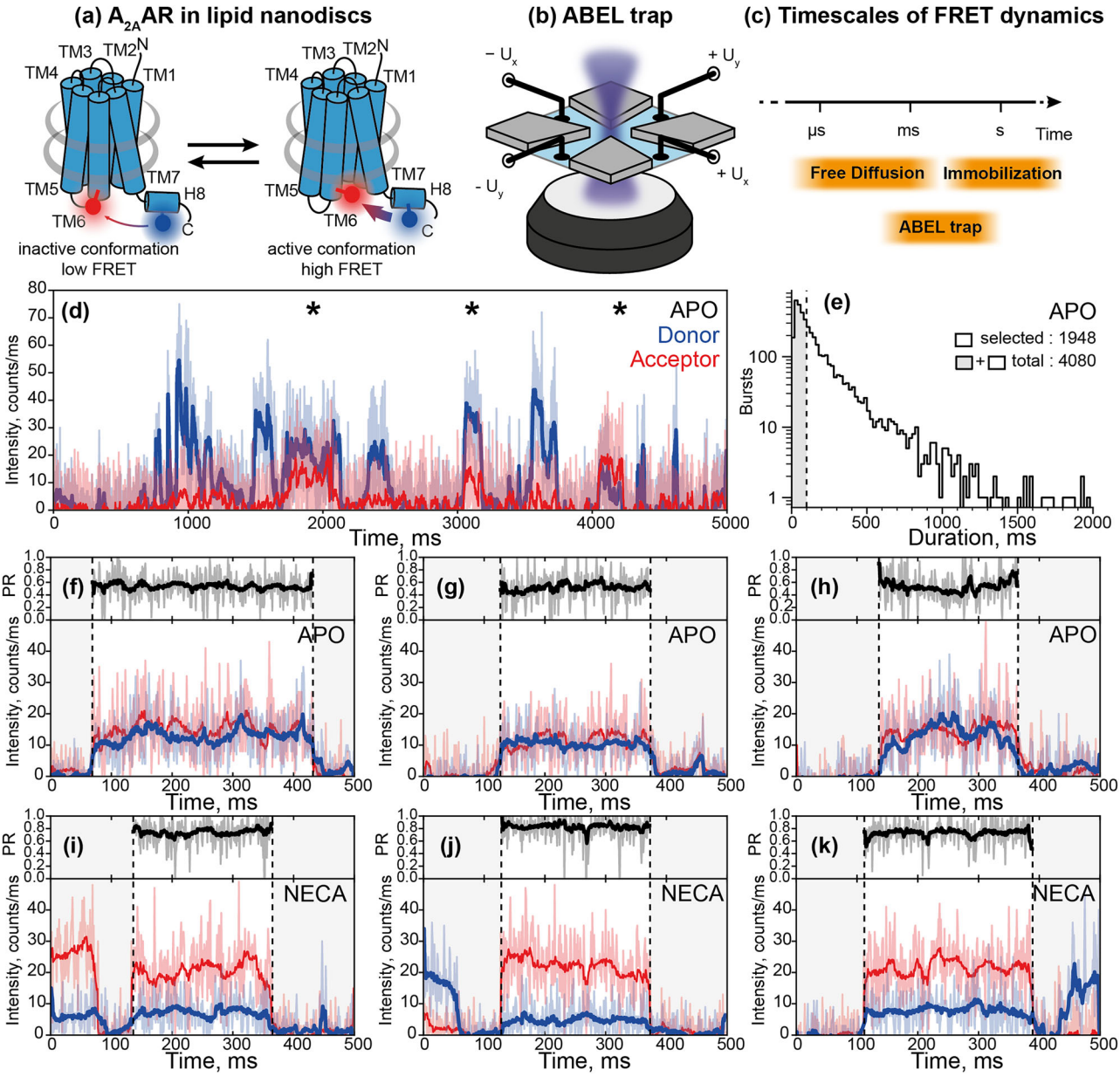

Fig. 1 | smFRET dynamics of individual A_{2A}ARs in the ABEL trap. a A_{2A}ARs were labeled with donor (Alexa488, blue circle) and acceptor (Atto643, red circle) fluorescent dyes at the intracellular tip of the transmembrane helix TM6 and the amphiphilic C-terminal helix H8 and were reconstituted in lipid nanodiscs (gray belts). The FRET efficiency in labeled A_{2A}AR increases upon receptor activation. **b** Sketch of the ABEL trap setup with four electrodes in the PDMS-based microfluidic chamber. The FRET donor fluorophore is excited by a fast-switching laser beam pattern, and the fluorescence of both donor and acceptor on individual receptors is collected through the objective of a custom-built confocal microscope. **c** The timescales of the structural dynamics observed using smFRET in the ABEL trap and the most common smFRET experiment modalities, i.e., confocal microscopy with freely diffusing molecules and TIRF camera-based microscopy with immobilized molecules. **d** Fluorescence traces in the donor (blue) and acceptor (red) channels were recorded for individual A_{2A}ARs held in solution by the ABEL trap. Background-corrected fluorescence traces were binned in 1-ms time-bins (thin semitransparent lines) and then smoothed using Chung-Kennedy filtering (thick lines). Fluorescence bursts with both donor and acceptor fluorescence are depicted with asterisks. **e** The histogram of the durations of the individual fluorescence bursts recorded for the apo A_{2A}ARs. The photon bursts shorter than 100 ms were excluded from the analysis (gray area). Out of the total 4080 bursts for apo A_{2A}ARs, 1948 bursts longer than 100 ms were selected and further filtered based on fluorescence intensity, yielding 1815 bursts for further analyses (see Supplementary Fig. 3, Supplementary Table 1). Exemplary fluorescence traces for the individual apo A_{2A}ARs (**f**–**h**) and A_{2A}ARs with agonist NECA (**i**–**k**). Donor (blue) and acceptor (red) fluorescence signals were plotted after binning with a 1-ms time-window and background subtraction (thin semitransparent blue and red lines). The areas outside of the selected fluorescence bursts are gray. For each 1-ms time-bin within bursts, the Proximity Ratio (PR; Eq. 1) was calculated (thin semitransparent black lines), and then, PR profiles were smoothened with Chung-Kennedy filtering (thick black lines)[109].

donor fluorophore with a continuous-wave laser at 491 nm and simultaneously recorded direct emission from the donor and FRET-induced emission from the acceptor. The sharp increases in the fluorescence in both channels manifested the detection of individual double-labeled receptors, followed by sharp decreases back to the background level when the receptors escaped from the trap, or photobleaching of the donor fluorophore occurred. The receptors with absent or photobleached acceptors, where donor fluorescence was not accompanied by a FRET signal, were excluded from the analysis. If the acceptor fluorophore was bleached during the observation time, the fluorescence traces up to the moment of photobleaching were

analyzed. For technical reasons, direct acceptor excitation could not be done, hence, we could not distinguish double-labeled molecules exhibiting no or low FRET from molecules labeled only with the donor. This bias in our measurements, potentially, leads to undersampling of low-FRET bursts in the analysis. However, previous smFRET experiments with freely-diffusing $A_{2A}AR$ molecules and dual-color ALEX excitation have shown that the fraction of $A_{2A}AR$ in the low-FRET state is minor (<20%) for apo and ligand-bound receptors, and likely represents non-functional or improperly folded receptors[68,72]. We performed diffusion analysis of individually trapped $A_{2A}AR$ embedded in MSP1D1 nanodiscs as described in the Methods section "Diffusion Analysis", and the resulting distribution of diffusion coefficients is very narrow, with a mean of 36 $\mu m^2\ s^{-1}$ and an SD of less than ±5% (Supplementary Fig. 2). The fluorescence intensities of individual molecules were predominantly distributed around a single peak, with no evidence of distinct subpopulations, with an average intensity of 20–30 photon counts per millisecond (sum of both color channels, averaged over the observation times; Supplementary Fig. 3, Supplementary Table 1). To exclude a few potential oligomers or aggregates, we removed receptors with total fluorescence intensities exceeding 40 photon counts per millisecond from all further analyses.

To quantify FRET efficiency changes within the observation time of individual $A_{2A}AR$ molecules and among various molecules in the ensemble, we calculated the Proximity Ratio (PR) as follows:

$$PR = I_A/(I_D + I_A) \quad (1)$$

where I_D and I_A are background-corrected fluorescence intensities of donor and acceptor, averaged either within 1-ms time-bins (bin-wise PR) or over the entire fluorescence burst from the individual receptor (burst-wise PR).

We compared the distributions of the burst-wise PR across different samples, including $A_{2A}AR$ in its ligand-free (apo) state as well as bound to either an antagonist ZM241385 or agonists NECA (5'-N-ethylcarboxamidoadenosine) or adenosine (Fig. 2b). In agreement with our previous studies with $A_{2A}AR$ labeled with the same dyes at the same labeling positions[68,72], the antagonist did not change PR, while the agonists increased PR compared to the ligand-free condition. Under all four conditions, the PR distributions were much wider compared to what could be expected from shot-noise-limited data, indicating $A_{2A}AR$ states that do not fully interconvert during the observation times of hundreds of milliseconds (Fig. 2b). These long-lived receptor's states can be related to the slow conformational dynamics of $A_{2A}AR$ observed in the experiments with immobilized receptors[69].

Variance analysis reveals moderate but significant conformational dynamics in $A_{2A}AR$

Under all measured conditions, ligand-bound or apo, the PR fluctuations within detection times of individual receptors were significantly higher than those expected from the shot noise limit (Fig. 2c). To make this comparison, we adapted the Burst Variance Analysis[73] approach to ABEL-FRET data and simulated the data for the "static heterogeneity" scenario with the same number and lengths of single-molecule fluorescence bursts, the same levels of total fluorescence signal and background, and the same PR distributions. In this simulation, each molecule was attributed an independent, constant PR, and the fluctuations were purely due to the shot noise (Fig. 2a). The PR fluctuations larger than the shot noise limit indicate conformational dynamics of $A_{2A}AR$ as well as complex photophysics of the fluorophores, or fluctuations of the background fluorescence.

Correlation-based analysis reveals slow dynamics and long-lived conformational states of $A_{2A}AR$

To analyze the time scales of the conformational dynamics observed in $A_{2A}AR$ by ABEL-FRET, we calculated the normalized autocorrelation function for the PR fluctuations as follows:

$$G(\tau) = \frac{<\delta PR_i(t)\cdot\delta PR_i(t+\tau)>_{t,i}}{<\delta PR_i(t)\cdot\delta PR_i(t)>_{t,i}} \quad (2)$$

where i and t indices correspond to the individual fluorescence bursts and time bins within them, respectively, and averaging is performed over all pairs of time bins t and $t+\tau$ from all bursts. The PR fluctuations $\delta PR_i(t)$ were calculated with a reference of PR averaged over all 1-ms time bins for all detected molecules:

$$\delta PR_i(t) = PR_i(t) - <PR_i(t)>_{i,t} \quad (3)$$

The normalized autocorrelation function equals 1 at lag time τ=0 (not shown in log-scale plots), and in essence, represents the fraction of total PR variance that remains correlated as the system's memory of its starting state fades over time lag τ. In the apo and ligand-bound $A_{2A}AR$, the autocorrelation is positive over the whole range of τ from the shortest binning time $\tau = 1$ ms to the longest $\tau = 300$ ms (Fig. 2d). The autocorrelation decreases almost linearly with $\log(\tau)$ in all apo or ligand-bound conditions. The positive autocorrelation in this analysis indicates the heterogeneity within the ensemble of $A_{2A}ARs$ in different receptor states, distinguished by PR. In an imaginary scenario of "static homogeneity", where all molecules have the same conformation and the PR fluctuations are due to the shot noise in the fluorescence data, such an analysis would result in the autocorrelation of zero for all $\tau > 0$. The zero autocorrelation would also be expected if the conformational dynamics of a protein are much faster than the 1-ms binning time used in the analysis (Fig. 2a, d).

In our autocorrelation-based analysis, the decrease of the autocorrelation over time indicates the conformational dynamics of $A_{2A}AR$ on this timescale. In a hypothetical scenario of a protein switching between two states with rate constants k_{12} and k_{21}, the autocorrelation curve is expected to be sigmoidal with a 50%-loss of the autocorrelation at the relaxation time of $\tau = (k_{12} + k_{21})^{-1}$, and approaching zero at much longer times. Alternatively, in the case of "static heterogeneity", where molecules have distinct static states with no inter-state switching, a positive autocorrelation that does not decrease with τ is expected (Fig. 2d). Based on our ABEL-FRET data, the case of "apparent static heterogeneity", where inter-state switching occurs on much longer timescales than the molecule's residence times within the ABEL trap region, is indistinguishable from the true "static heterogeneity" (Fig. 2a). Notably, at large time lags $\tau > 100$ ms, the correlation-based analysis is increasingly dominated by rare long-lived trapping events, resulting in deviations of correlation curves from their expected horizontal trends for the simulated "static heterogeneity" scenario. These artifacts mark the range of τ in which correlation-based analysis becomes unreliable.

The low starting levels of the autocorrelation curves in our analysis can potentially be affected by the shot noise in the data, or by the fast sub-millisecond dynamics of the receptors (Fig. 2d). In the apo and ligand-bound $A_{2A}AR$, these levels are ~20%, indicating that 80% of the variance in the PR data is not correlated between consecutive 1-ms time bins. To test the fast conformational dynamics hypothesis, we performed computer simulations of the "static heterogeneity" scenario, where the shot noise is the only source of the PR fluctuations within the individual trapping events (Fig. 2a, d). In these simulations, we obtained similar starting levels of the autocorrelation, suggesting that the low starting values of the autocorrelation are due to shot noise rather than fast conformational dynamics.

The PR autocorrelation curves measured for the apo and ligand-bound $A_{2A}ARs$ revealed a substantial residual correlation between PRs measured with a time delay of hundreds of milliseconds, indicating long-lived receptor's states (Fig. 2d). This high residual autocorrelation further supports the "static heterogeneity" scenario, where molecules have distinct conformations that remain unchanged during trapping times, as a good approximation for $A_{2A}AR$. The subtle but significant decrease in the PR correlation measured for $A_{2A}AR$ does not show clear sigmoidal transitions

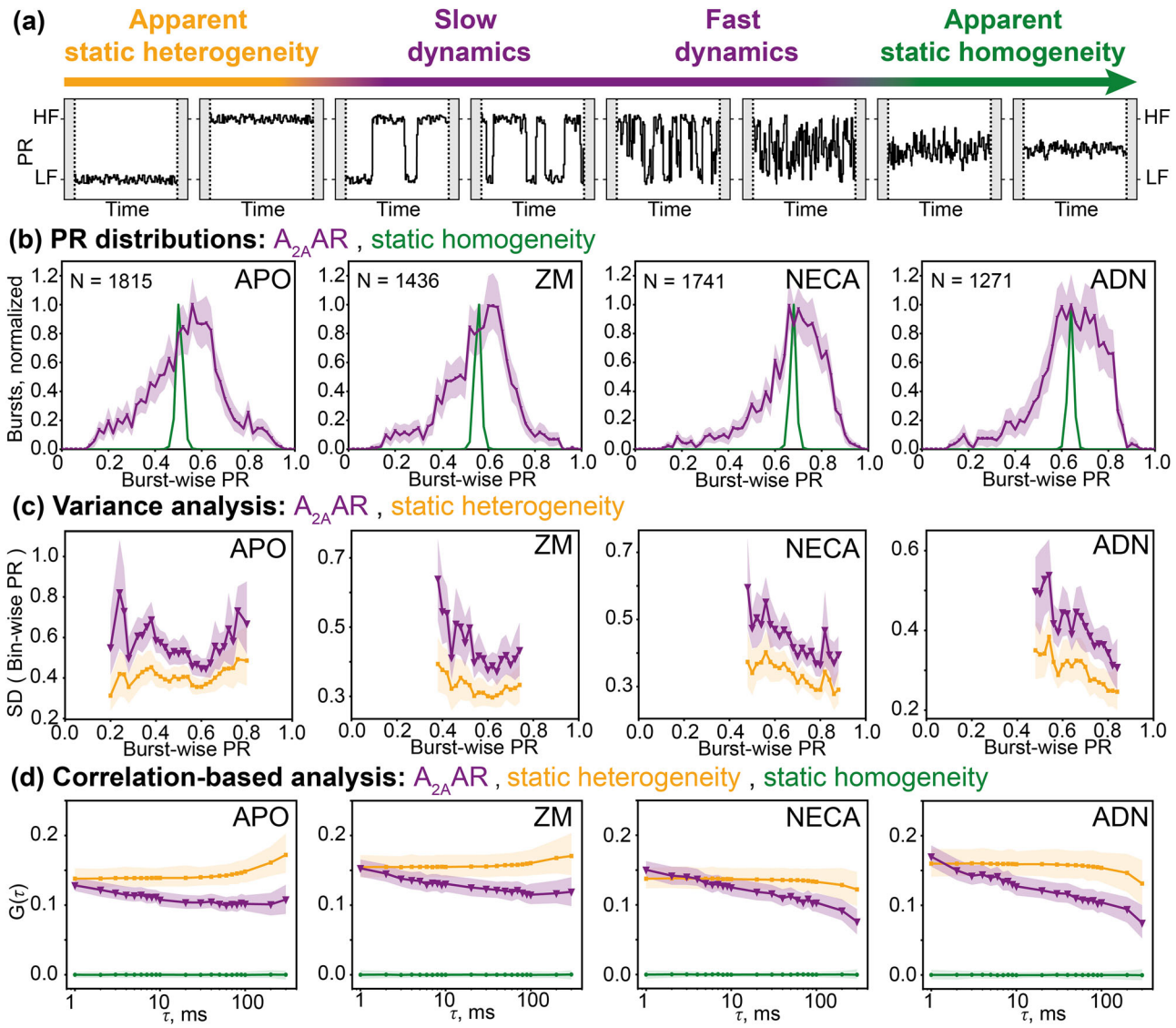

Fig. 2 | Burst-wise analysis of the structural heterogeneity and dynamics of A_{2A}AR. a Schematic drawings of the PR traces expected for a molecule switching between low-FRET (LF) and high-FRET (HF) states. Left, "apparent static heterogeneity" scenario: if the switching is too slow to occur within the observation time of individual molecules, the data is indistinguishable from the "static heterogeneity" scenario, where low-FRET and high-FRET species do not interchange. Right, "apparent static homogeneity" scenario: if the switching is fast enough to average over the binning time of the experiments, the data is indistinguishable from the "static homogeneity" scenario, where all molecules have the same PR that remains constant over time. **b** Experimental distributions of the burst-wise PR measured for A_{2A}AR without ligands (APO, $N = 1815$ bursts), with antagonist ZM241385 (ZM, $N = 1436$ bursts), with agonist NECA (NECA, $N = 1741$ bursts), and with agonist adenosine (ADN, $N = 1271$ bursts) are shown (purple lines). Simulated distributions for the "static homogeneity" scenario are also given (green lines) to show the expected broadening of the PR distributions due to shot noise. In the "static homogeneity" simulations, the ground-truth burst-wise PR matches the ensemble-averaged burst-wise PR in the A_{2A}AR data. **c** Standard deviations of the PRs measured in 1-ms time-bins were averaged in the groups of bursts equally spaced along the burst-wise PR axis, and were plotted for the apo and ligand-bound A_{2A}ARs (purple lines) and the simulated "static heterogeneity" scenario (orange line). In the "static heterogeneity" simulations, the distribution of the PR matches those of the A_{2A}AR data. PR bins with less than 20 bursts were not analyzed. **d** Autocorrelation functions for the PRs calculated in 1-ms time-bins are plotted for the apo and ligand-bound A_{2A}AR (purple lines), and for simulated "static heterogeneity" (orange) and "static homogeneity" (green) scenarios. In the simulated data, the numbers of bursts, their durations, and the levels of the shot noise match those of the experimental data for A_{2A}AR shown on the same panel. The 95% confidence intervals were obtained via statistical bootstrapping (shaded colored areas)[110].

within the 1–300 ms time scale and, most probably, indicates either complex minor multi-state conformational variability on the observed time scales or the onset of slower dynamics with exchange relaxation times longer than 300 ms.

Upon structural changes in A_{2A}AR, PR values vary due to alterations in the distance between the dyes or their relative orientation, resulting in true FRET changes. Additionally, FRET-independent alterations in brightnesses of individual dyes, e.g., due to changes in their local environment, can also manifest as PR variations. To disentangle the contributions of FRET changes and other processes, we analyzed correlation functions for donor and acceptor fluorescence intensities and their sum (Supplementary Fig. 4). Under all apo and ligand-bound conditions, intensities in donor and acceptor channels were anticorrelated, indicating that FRET changes played a major role in the observed heterogeneity in PR values. However, the indications of FRET-independent fluorescence changes in the A_{2A}AR were also evident, i.e., a decrease in the cross-correlation function G_{DxA} at 1–10 ms delay times and a decrease in autocorrelation functions without a corresponding increase in cross-correlation at 10–100 ms. These observations suggest that FRET changes discriminate the long-lived A_{2A}AR states and underlie the PR variability across many molecules, while other

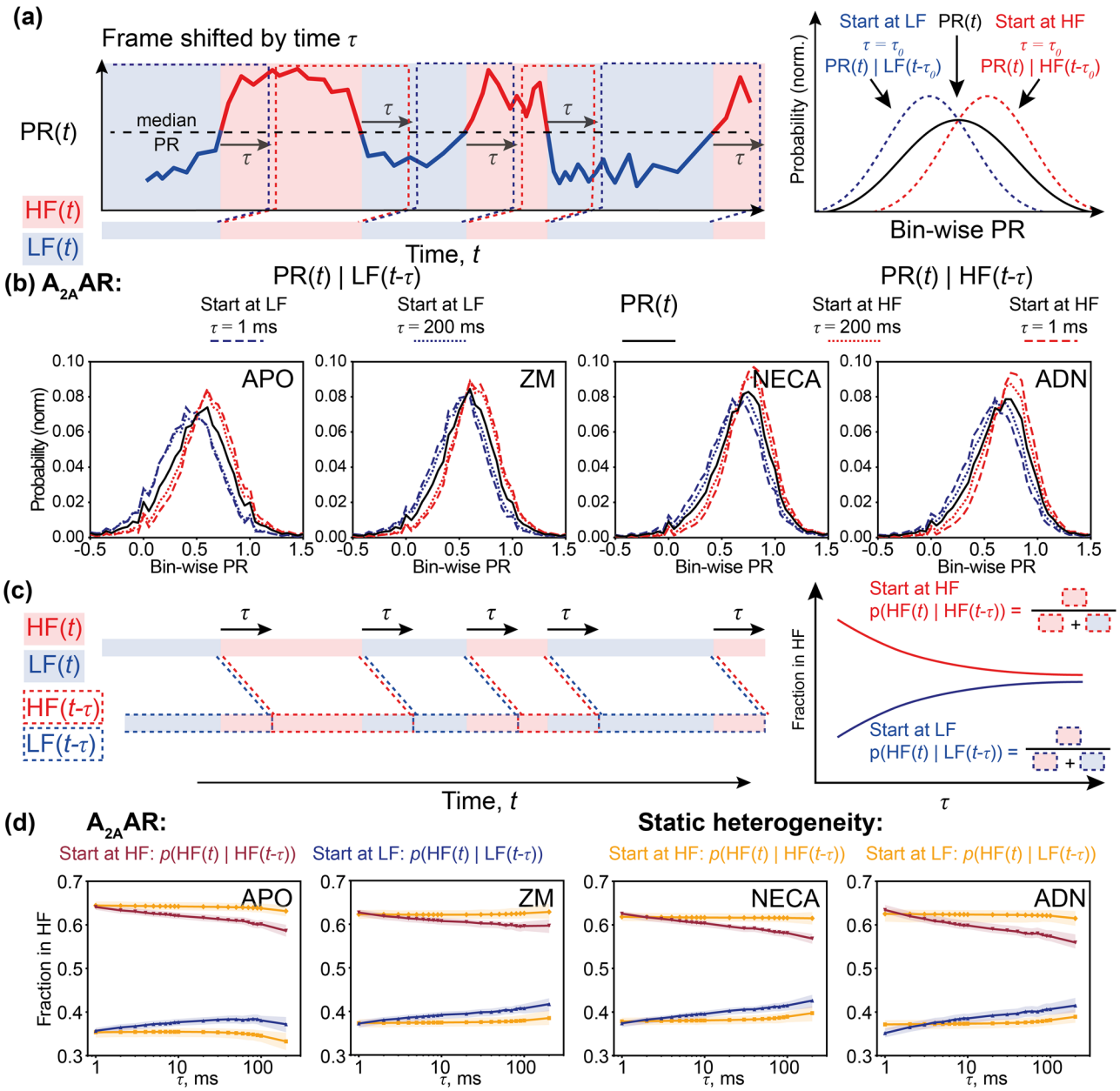

Fig. 3 | Recurrence analysis of the PR distributions. a In the time-trace of the bin-wise PR (thick line), positive (red areas, above median PR) and negative (blue areas, below median PR) fluctuations are assigned to the high-FRET (HF) and low-FRET (LF) regions, respectively. For a given time delay τ, the distributions of bin-wise PR are plotted for the regions shifted by τ over the time axis from the HF regions (PR(t) | HF(t-τ), dashed red lines) or from the LF regions (PR(t) | LF(t-τ), dashed blue lines). The shifts of these distributions from the general bin-wise distribution of PR (black line) indicate a higher than random probability of finding the protein in the same state for the time points t-τ and t. **b** Distributions of the bin-wise PR in the regions shifted from the LF ("Start at LF") or HF ("Start at HF") regions by time delays τ = 1 ms and τ = 200 ms are shown for the apo and ligand-bound A_{2A}AR. The general distributions of bin-wise PR are shown in black. **c** The conditional probability of observing the positive fluctuation in PR at the time t (red areas), given that earlier, at the time t-τ, a positive fluctuation was also observed (dashed red contours), is calculated as a function p(HF(t) | HF(t-τ)) of τ (solid red line). Similarly, the probability of the positive fluctuation in PR at time t, given that a negative fluctuation was observed at time t-τ (dashed blue contours), is calculated as a function p(HF(t) | LF(t-τ)) of τ (solid blue line). On the right, two curves converge to the same value at times much longer than the inter-state exchange relaxation time of the target molecules. **d** Two conditional probabilities of the positive fluctuation in PR are plotted for the apo and ligand-bound A_{2A}AR. Two orange lines show the same curves for the simulated "static heterogeneity" scenario (p(HF(t) | HF(t-τ)) - higher line; p(HF(t) | LF(t-τ)) - lower line). The 95% confidence intervals were obtained via statistical bootstrapping (shaded colored areas)[110].

FRET-independent processes contribute to PR fluctuations within observation times of individual A_{2A}AR molecules.

Long-lived states of A_{2A}AR are confirmed by the recurrence analysis on the PR distributions

To further investigate the long-lived A_{2A}AR states, we compared how the PR distributions change over time for the A_{2A}AR molecules that at a certain time-point exhibited a PR above ("high-FRET") or below ("low-FRET") the ensemble-averaged median (Fig. 3a, b). Under all four apo and ligand-bound conditions, A_{2A}ARs with a higher-than-average PR in a 1-ms time bin exhibit, in general, a higher-than-average PR in the subsequent 1-ms time bin. This trend is preserved even for the time delay of 200 ms, with the PR distributions barely shifting towards the "equilibrium" of the ensemble distribution. An apo A_{2A}AR molecule that showed a "high-FRET" PR in a given time bin has 65% and 59% probabilities of showing the "high-FRET" PR 1 ms and 200 ms after the initial observation, respectively (Fig. 3c, d).

Both probabilities are significantly above a random 50% value expected if the time delay between two data points is much longer than the typical timescale of the conformational dynamics.

The probability of observing "high-FRET" PR after it was once observed significantly decreases with the time delay between two data points for the apo and ligand-bound $A_{2A}AR$ (Fig. 3d). This decrease indicates moderate but significant conformational dynamics of $A_{2A}AR$ on the 1–200 ms time range. For reference, we also examined simulations of the "static heterogeneity" scenario, where molecules have distinct conformations that remain unchanged over the trapping time, and the PR variations are due to the shot noise in the fluorescence data. The probability of recording a "high-FRET" PR 1-ms after it was once recorded is similar in "static heterogeneity" scenario to what we observe for $A_{2A}AR$, but this probability does not decrease for the longer time delays τ. Notably, the similar starting levels in the experimental data and simulations indicate that the shot noise in the data renders the sub-millisecond fast receptors' dynamics invisible in our experimental ABEL trap setup.

In summary, our findings demonstrate that $A_{2A}AR$ exhibits only moderate deviation from the "static heterogeneity" scenario, with a high probability of detecting the receptor in the same "state" in the beginning and the end of the trapping time of hundreds of milliseconds. Using the ABEL-FRET, we bridged the gap between previous studies using confocal smFRET with freely diffusing receptors[67,68], where the sub-millisecond conformational dynamics were investigated, and the TIRF-based measurements with the immobilized receptors[69,70], shedding light on the dynamics on the time scale of seconds. In this study, the fast dynamics of $A_{2A}AR$ could not be resolved due to the shot noise in the fluorescence data and the microsecond motion of the laser focus in the ABEL trap, and were averaged out within 1-ms time binning. The slow dynamics contributed to subtle yet statistically significant deviations from the "static heterogeneity" scenario observed in our data. We did not observe any characteristic dynamics in $A_{2A}AR$ on the time scales from milliseconds to hundreds of milliseconds - neither the autocorrelation function nor the probability of detecting the same-sign PR fluctuation showed a sigmoidal decrease within the observed time scale.

Discussion

Using the ABEL-FRET approach, we monitored the conformational changes in the individual $A_{2A}ARs$ reconstituted in lipid nanodiscs during trapping times of 0.1–2 s (Fig. 1). In previous ABEL trap studies, three GPCRs, the β_2-adrenergic receptor (β_2AR[46]), the β_1-adrenergic receptor (β_1AR[74]), and the neurotensin receptor 1 (NTSR1[47]), were reconstituted in detergent micelles, lipid nanodiscs, and SMALPs, respectively, and trapped in solution for up to a few seconds. In addition to GPCRs, another membrane protein, F_oF_1-ATP synthase, was previously FRET-labeled and reconstituted in proteoliposomes for ABEL-FRET[75–77] yielding comparable observation times of a few seconds for the conformational dynamics in the 10 to 100 ms time range. The nanosecond photophysics and energy transfer of other membrane proteins studied in the ABEL trap include the light-harvesting complex LH2 in detergent micelles[78]. Lipid nanodiscs with a controlled diameter and lipid composition provide a native-like lipid bilayer environment and maintain functionality and high stability for a variety of reconstituted protein targets[79]. Lipid nanodiscs have been widely used for studying membrane protein structure and function[80] (e.g., via NMR, DEER, or cryo-EM) and for drug screening[81]; therefore, their temporary immobilization by ABEL trapping opens the way for many cross-method correlational studies.

A recent study using ABEL trap and DEER demonstrated that class A GPCRs can dimerize in lipid nanodiscs[74]. Because of the low labeling efficiency in our experiments, we cannot exclude the presence of $A_{2A}AR$ dimers based on our spectroscopic data. Several independent studies have reported that $A_{2A}AR$ incorporated into MSP1D1 nanodiscs using protocols comparable to ours is a monomer, as demonstrated by SDS–PAGE analysis[82] and analytical ultracentrifugation[83]. Moreover, even larger MSP1E3 nanodiscs have been shown to accommodate only a single $A_{2A}AR$ molecule[65].

Fast sub-millisecond conformational dynamics of $A_{2A}AR$ were previously observed by smFRET[68], PET-FCS[67], and NMR[62,63,65], with $A_{2A}AR$ reconstituted in lipid nanodiscs or detergent micelles. In this study, we could not observe the conformational dynamics of the $A_{2A}ARs$ on this timescale, because within 1 ms, only few fluorescence photons were detected from individual receptors, i.e., about 20 to 30 photons (Supplementary Fig. 3, Supplementary Table 1). In addition, the fluorescence intensities measured in the ABEL trap fluctuate on the sub-millisecond timescale due to rapid laser scanning with an 8-kHz repetition rate for the full knight's tour across the 32-point pattern within the trapping area (Supplementary Fig. 5). To counteract the shot noise, we used the 1-ms binning in the smFRET analysis, and the sub-millisecond dynamics were averaged within the individual time bins.

The long-lived structural states of $A_{2A}AR$ with dwell times longer than milliseconds were observed in previous NMR[63–66,84–86] and smFRET experiments[67,68]. In the smFRET-based studies[67,68], the individual $A_{2A}ARs$ were observed for several milliseconds until the freely-diffusing receptors left the focal spot of the microscope. With the ABEL trap, we extended the observation time of the individual receptors to 2 s (Fig. 1e). On this timescale, we see only minor changes in the FRET efficiencies in individual $A_{2A}AR$ molecules, with a high probability of each molecule remaining in the same state throughout the photon burst (Fig. 1f–k, Fig. 2c, d, 3c, d). Thus, we can update the previous estimates of the dwell times for the long-lived $A_{2A}AR$ states observed by smFRET by two orders of magnitude, from milliseconds to hundreds of milliseconds. The existence of long-lived states with dwell times exceeding 100 ms is also supported by the recent NMR-based study with $A_{2A}AR$ reconstituted in lipid nanodiscs[86]. The minor, yet significant, dynamics on the 1 to 300 ms time scales that we observed using the correlation-based analysis (Fig. 2d) and the recurrence analysis (Fig. 3c, d) of the PR distributions can be related to the sub-second dynamics of the $A_{2A}ARs$ previously measured via NMR[64,66] or is an onset of even slower dynamics. As dye photophysics is inherently challenging to smFRET analysis, we cannot completely exclude that long-lived photophysical states of the dyes contribute to the heterogeneity observed in the FRET efficiency distributions for the double-labeled $A_{2A}AR$[87,88]. Long-lived photophysical states of the dyes with distinct fluorescent lifetimes and emission spectra were previously shown for commercial dyes using the ABEL trap[88].

Using molecular dynamics simulations, we previously showed that the FRET changes observed upon the activation of the $A_{2A}AR_{L225C/Q310C}$ can be due to the outward movement of the intracellular tip of TM6, followed by the movement of the dye attached to L225C$^{6.27}$ toward the G protein binding cavity[68]. Using the ABEL trap, we observed long-lived FRET-states of $A_{2A}AR$ with dwell times exceeding 200 to 300 ms (Fig. 2d, Fig. 3d). We hypothesize that these states represent slow structural rearrangements of the intracellular part of the receptor around the major active and inactive conformations. These slow rearrangements might be functionally important for the recognition of the G protein and can be linked to the slow, minutes-long rearrangements in the structure of G protein bound to $A_{2A}AR$, which was previously observed via HDX MS[89].

The slow seconds-long switching between the $A_{2A}AR$ conformations was previously monitored using single-molecule fluorescence microscopy with up to 0.1 s temporal resolution using immobilized $A_{2A}ARs$ reconstituted in nanodiscs[69,70]. The long-lived states observed in our experiments can be related to these previously reported states. The direct comparison between the two single-molecule studies is challenging because different strategies were used to follow the conformational dynamics of the receptor. In the studies of Wei et al.[69,70], the structural changes around the intracellular tip of TM7 were probed with the environment-sensitive dye Cy3, while in our study, the movement of TM6 was probed via the FRET pair of dyes on TM6 and the C-terminal helix H8 (Fig. 1a). We hypothesize that the same global conformational rearrangements in $A_{2A}AR$, occurring on the timescales of seconds and involving both TM6 and TM7, influence the fluorescence readouts in our study and in the study of Wei et al.[69,70].

Using insights from our ABEL-FRET study, we update the action model of the $A_{2A}AR$ that we introduced in our previous smFRET study[68]. As

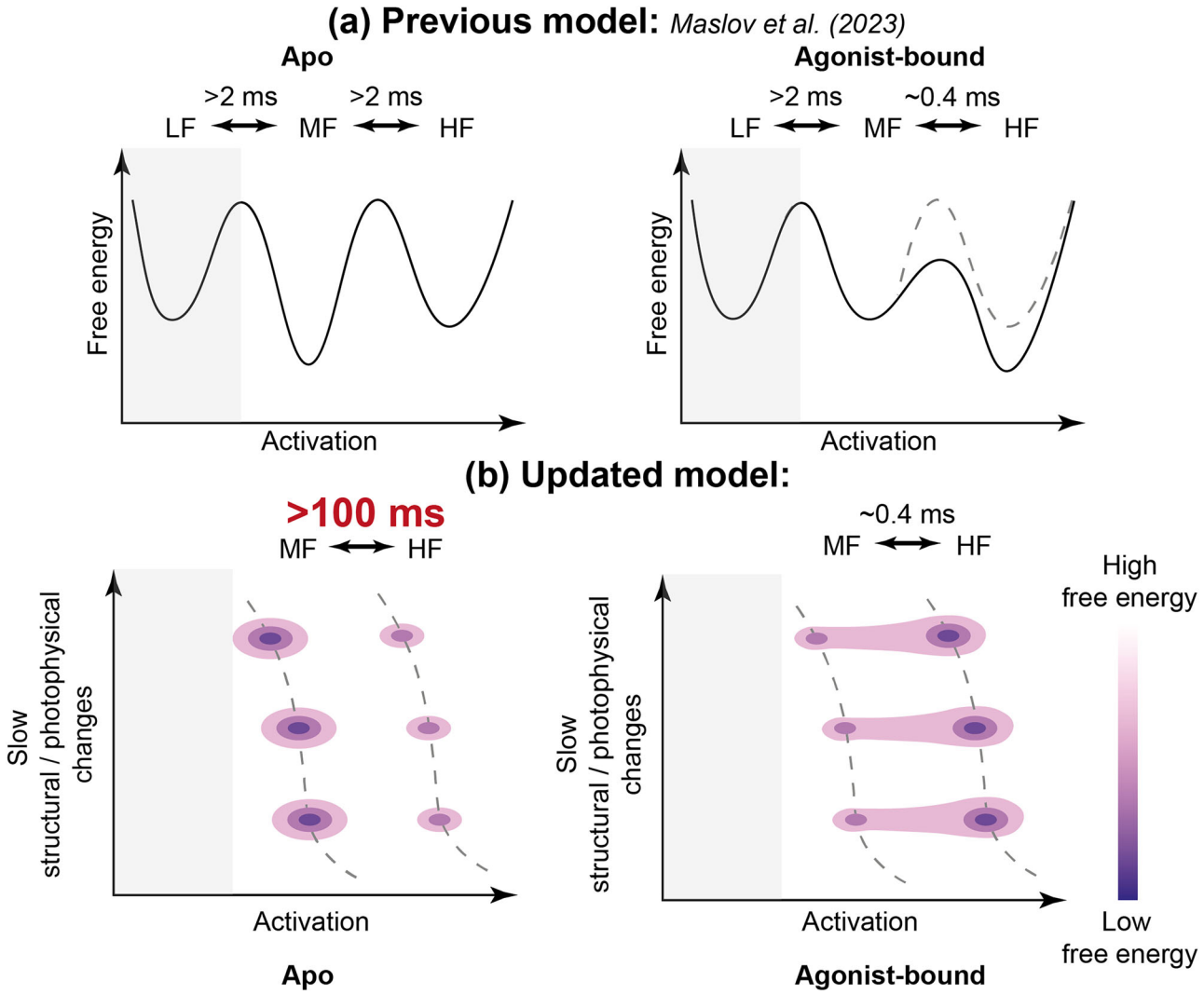

Fig. 4 | Updated action model of the A_{2A}AR. a A previously proposed three-state action model of the A_{2A}AR and corresponding energy landscapes for the apo and agonist-bound A_{2A}AR[68]. **b** Updated scheme of two-dimensional energy landscapes shows long-lived sub-states within inactive-like state with intermediate FRET efficiency (MF) and active-like state with high FRET efficiency (HF). We did not include a state with the lowest FRET efficiency (LF, gray areas) in our updated model, as it was the least populated and assigned to non-functional or improperly folded receptors in the previous study[68] and, in the current study, it was not observed as it was indistinguishable from molecules without active acceptor dyes. We updated the estimate of exchange time between MF and HF in apo A_{2A}AR from >2 ms proposed previously[68] to >100 ms.

in the initial three-state model, the active-like state with the highest FRET efficiency (HF) is the most populated in agonist-bound A_{2A}ARs and the inactive-like state with the intermediate FRET efficiency (MF) is the most populated in apo and antagonist-bound A_{2A}ARs (Fig. 4). The previously observed A_{2A}AR state with the lowest FRET efficiency (LF) was the least populated under all apo or ligand-bound conditions and was assigned to non-functional or improperly folded receptors. In our ABEL-FRET measurements, we directly excited only the donor, but not the acceptor fluorophores. Therefore, the molecules with low FRET efficiencies were indistinguishable from those without active acceptor dyes and were not analyzed. Since the LF state was the least populated state, which likely does not describe a functional receptor, and was not observed in ABEL-FRET experiments, we did not include it in our updated model. We showed that agonist-bound A_{2A}ARs switch between MF and HF states with an exchange time of ~0.4 ms, while in apo and antagonist-bound A_{2A}ARs, this switching is slower (>100 ms). We use a schematic two-dimensional energy landscape to illustrate this fast agonist-induced switching between MF and HF, together with long-lived heterogeneities within individual states revealed via ABEL-FRET. In this updated A_{2A}AR energy landscape, the inter-state energy barrier between MF and HF is low in the agonist-bound A_{2A}ARs and high in the apo and antagonist-bound A_{2A}ARs, and the intra-state energy barriers among the MF and HF sub-states are high under all apo and ligand-bound conditions.

Our study showed that the ABEL-FRET approach can be used for the studies of the conformational dynamics of membrane proteins reconstituted in lipid nanodiscs. ABEL-FRET measurements bridge the gap in the time scales, where conformational dynamics in the A_{2A}AR were previously monitored by single-molecule fluorescence microscopy, i.e., from 1 ms, the near-maximum time observed in the measurements with freely diffusing molecules[67,68], to 100 ms, the shortest temporal resolution of the previous study with immobilized A_{2A}AR[69,70]. Our measurements revealed no pronounced conformational dynamics in this 1–300 ms region, thus refining the estimate for the dwell times of the long-lived states previously observed in the freely-diffusing receptors, and linking them with states observed in immobilized receptors with dwell times of seconds.

Key factors for ABEL trapping include: (1) using fluorophores that are bright (i.e., high quantum yield) and photostable (with minimal blinking, resistance to photobleaching, and limited spectral fluctuations); (2) minimizing fluorescence background from the buffer and sample chamber to ensure a good signal-to-background ratio; (3) coating the surfaces of the

sample chamber to prevent sticking in the trapping region; and (4) increasing the trapping region to sizes as large as $4 \times 4\ \mu m^2$ for trapping of small molecules such as single fluorophores. Any concerns regarding local heating of ABEL-trapped molecules or potential effects of fast-changing electric fields on conformational dynamics have to be addressed experimentally. For example, six independent smFRET studies of different FRET-labeled F_oF_1-ATP synthase mutants with freely-diffusing enzymes[90–92] and with ABEL trapped enzymes[75,77,93] yielded similar mean ATP hydrolysis rates. The averaged reaction times ranged from 6 to 19 ms per hydrolyzed ATP molecule and exhibited very broad distributions for the individual enzyme kinetics in all measurements. The comparison indicated that the ABEL trapping conditions had negligible effects on membrane enzyme kinetics, and validated the impact of specific mutations on single-enzyme kinetics.

Several technical advancements hold promise for enhancing both the temporal resolution and the maximum trapping duration in future ABEL-FRET studies, thereby broadening the accessible timescale for monitoring the structural dynamics of GPCRs and other membrane proteins, but also soluble proteins, nucleic acids, and inorganic nanoparticles[41,94–96]. For example, the use of all-quartz ABEL trap microfluidic devices can significantly reduce background fluorescence[97], while self-healing fluorescent dyes[98,99] or DyeCycling approaches[28] improve dye photostability and effective brightness, thus extending observation times. Specific coatings of the all-quartz microfluidics allow ABEL trapping of both charged and non-charged molecules in buffers with varying ionic strengths by switching between electrophoretic and electroosmotic force contributions[41]. Fluorescence lifetime measurements with pulsed lasers in the ABEL trap can delineate sub-millisecond dynamics from the instrumental fluorescence fluctuations due to rapid laser scanning of the trapping area[100,101]. Furthermore, multiplexed readouts - such as fluorescence lifetime and anisotropy measurements, or assessments of particle diffusion coefficients and electrokinetic mobility - can uncover receptor states that remain indistinguishable using conventional FRET metrics[42,102,103]. Collectively, these innovations highlight the strong potential of ABEL-FRET for comprehensive, high-resolution studies of conformational dynamics in membrane proteins and other systems.

Methods

A_{2A}AR sample preparation

The double mutant $A_{2A}AR_{L225C/Q310C}$ sample used here was prepared and functionally characterized in our previous study[72]. In that study, the human ADORA2A gene encoding A_{2A}AR (2-316 aa) with an N-terminal hemagglutinin signal peptide (MKTIIALSYIFCLVFA), FLAG-tag (DYKDDDDK), and a linker (AMGQPVGAP), mutations L225C$^{6.27}$ and Q310C$^{8.65}$, and C-terminal 10 X His-tag was expressed in *Spodoptera frugiperda* Sf9 cells (Novagen, USA, cat. 71104). The protein was labeled with Atto643-maleimide and Alexa488-maleimide in crude membranes, solubilized in DDM/CHS (n-dodecyl-b-D-maltoside/cholesteryl hemisuccinate), purified on the TALON resin, and reconstituted in lipid nanodiscs (MSP1D1, POPC:POPG 7:3). The sample in 25 mM HEPES pH 7.5, 150 mM NaCl was supplemented with 40% glycerol, aliquoted, flash-frozen in liquid nitrogen, and stored at −80°C. The purity and homogeneity of the sample were confirmed by SDS-PAGE and analytical SEC (Supplementary Fig. 1a, b). The labeling efficiencies were 16% for Alexa488 and 12% for Atto643. The ligand-induced changes in the thermal stability of the receptor were demonstrated via a TSA (Supplementary Fig. 1c).

Custom-designed confocal ABEL-FRET setup

All smFRET ABEL trap experiments were conducted on a modular home-built confocal microscope system as described before[40,47,75–77]. A PDMS-glass sample chamber was held on a piezo-driven stage (P-527.3CD, Physik Instrumente, Germany) incorporated into an inverted microscope (IX71, Olympus). A linearly-polarized continuous-wave 491-nm laser (Calypso, Cobolt, Sweden) was set to a 32-point Knight's tour laser focus pattern at an 8 kHz scanning speed per full pattern by two electro-optical beam deflectors (EOD, M310A, Conoptics, USA). The laser power was attenuated to 34 μW in the focal plane. The size of the laser focus pattern in the focal plane was $2.34 \times 2.34\ \mu m^2$.

The excitation and detection beam paths both passed through an oil immersion objective (60x, PlanApo N, oil, NA 1.42, Olympus, Germany). A dichroic mirror (zt 488 RDC, AHF, Germany) separated the detected fluorescence from the excitation laser. A pinhole (200 μm) in the image plane of the tube lens optimized the signal-to-noise ratio. A dichroic beam splitter (HC BS 580i, AHF) spectrally separated the donor and acceptor fluorescence signals before two single photon counting avalanche photodiodes (APD, SPCM-AQRH 14, Excelitas, USA). A bandpass (ET 535/70, AHF, Germany) and a longpass (LP 594, AHF, Germany) filter further determined the precise wavelength detection range for the donor and acceptor channels, respectively. All filters were chosen to maintain non-polarizing fluorescence detection conditions. A time-correlated single-photon counting (TCSPC) module (SPC-180NX with router HRT-82, Becker & Hickl, Germany) recorded arriving photons in the FIFO mode with software SPCM (version 8.9).

A field programmable gate array module (FPGA, PCIe-7852R, 80 MHz operation frequency, National Instruments, USA) operated the high voltage controllers (7602 M, Krohn-Hite Corporation, USA) of the EODs and the feedback voltage amplifier (built in-house, $|VPP| = 20$ V) to deliver electric fields via four platinum electrodes for counter-acting the molecule's Brownian motion. An implemented Kalman filter correlated the detected photon signals to the scanning pattern positions and estimated the particle trajectory. The original control software (Labview, National Instruments) was provided by A. Fields and A. E. Cohen[40] and modified[47,76] to match our hardware configuration and to implement the Knight's tour pattern.

ABEL-FRET measurements

Disposable microfluidic chambers for the ABEL trap were prepared from structured PDMS and glass as described in Heitkamp et al.[75] using the published design on a borosilicate glass wafer[76,104]. PDMS with a ratio of 10:1 polymer:hardener was cured for 48 h at 50 °C (Sylgard 184 elastomer, Dow, Midland, MI, USA). Holes for the electrodes in the PDMS part were punched using a sharpened needle. PDMS chips were sonicated in pure acetone, rinsed with deionized water and dried in a nitrogen stream. PDMS and 32×24 mm cover glasses with defined thickness (#1.5) were plasma-etched for 90 s and then bonded for 3 min to form a sample chamber.

Aliquots of labeled $A_{2A}AR_{L225C/Q310C}$ reconstituted in nanodiscs were thawed on ice, and the receptor was diluted in a buffer containing 10 mM NaCl, 20 mM HEPES pH 7.5 to a final concentration around 50 pM. Reduced salt concentration (10 mM NaCl) was chosen to minimize electrostatic screening and thus to improve ABEL trap performance. For ligand binding, receptors were pre-incubated on ice with 10 μM ZM24138, 10 μM NECA, or 100 μM adenosine for 10 min. We filled 10 μL of the analyte solutions into the PDMS/glass chamber of the ABEL trap. The sample chamber was exchanged with fresh sample every 25 min. For each apo or ligand-bound condition, at least three ABEL-FRET recordings were performed, each with new disposable microfluidic chamber and new protein aliquot from the same purification and labeling batch. For each condition, measurements were performed on at least 2 different days.

Burst selection

We analyzed the time traces of the fluorescence intensity in the donor and acceptor channels using a customized version of the "Burst Analyzer" software[105] (version 3.4.1; Becker & Hickl) with a 1-ms time binning. Fluorescence bursts were manually marked using stepwise rises of 25–40 photon counts per millisecond in the total fluorescence count rates as the beginning of the successful trapping events and stepwise drops back to the background fluorescence level as the end of the trapping events. The mean background levels were around 10–15 photon counts per millisecond for the donor channel and 20 to 25 photon counts per millisecond for the acceptor channel, caused by luminescence from PDMS and the cover glass.

To exclude the receptors without acceptor dyes or with photophysically inactive acceptors, only the photon bursts showing step-wise rise and decrease in the acceptor channel above the background level were selected. The acceptor blinking and bleaching events within a burst manifested in sharp decreases of the fluorescence in the acceptor channel to the background level—in these cases, the bursts were split into parts with the uninterrupted acceptor fluorescence. The background had to be subtracted for each photon burst individually because the background decreased on both channels in a time-dependent manner.

After the manual burst selection, bursts were removed from the subsequent analysis if the fluorescence intensity, combined from the two detection channels and averaged over the burst duration, exceeded 40 photon counts per millisecond or if a burst was shorter than 100 ms.

Diffusion analysis

The diffusion analysis was performed using the data from the ABEL trap's Field-Programmable Gate Array (FPGA). A total of 64 bursts with >100 ms trapping time were analyzed (Supplementary Fig. 2). During ABEL trapping, the FPGA recorded the applied electrode voltages and photon counts as time series with millisecond resolution for subsequent diffusion analysis. These voltage pulses counteract the Brownian motion and redirect the molecule's motion back to the center. A virtual diffusion path was reconstructed using the molecule's position probability by the Kalman filter as described previously[40], and two-dimensional MSD (mean squared displacement) analysis was performed on the virtual diffusion trajectory to obtain the diffusion coefficient of the trapped molecule[106,107]. The required mean lateral beam waist information $w_0 = 0.6$ µm was obtained by FCS with rhodamine 110 in H_2O with a fixed laser focus position on the same day of the ABEL trap recordings.

Computer simulations and statistical bootstrapping

We used *in silico* photon re-coloring to simulate burst data under two scenarios: "static homogeneity" and "static heterogeneity". In both cases, PR remains constant over time within each burst, and the numbers of bursts, their durations, and the shot noise levels mirror those observed in the experimental data. In the "static homogeneity" scenario, all bursts share the same burst-wise PR that matches the average PR across all 1-ms time-bins in the experimental data. In the "static heterogeneity" scenario, the distribution of the burst-wise PR matches those of the experimental data.

For each experimental burst, we simulated its "static homogeneity" and "static heterogeneity" re-colored versions that have the same number of 1-ms time-bins. In each k-th time-bin of a simulated burst, the total number of photons $I(k)$ equals the total uncorrected photon count in the corresponding k-th time-bin of the experimental burst. The assignment of photons to donor or acceptor channels is then randomized according to the scenario. We re-colored the background photon counts, assuming a constant total number of background photons across all 1-ms time-bins within a burst. For background photon counts, the number of photons in the donor and acceptor channels were simulated as a binomially distributed variable, based on the ratio of background fluorescence intensities in the acceptor and donor channels in a given burst, determined during burst marking. For background-corrected photon counts, the number of photons in the donor and acceptor channel was simulated as a binomially distributed variable according to the ground-truth PR of the simulated burst, which was determined by the chosen scenario. In the "static homogeneity" scenario, the ground-truth PR for each simulated burst equals the mean PR averaged across all 1-ms time-bins in all experimental bursts. In the "static heterogeneity" scenario, it equals the PR measured in the burst before re-coloring. After re-coloring, the fluorescence intensities of the simulated bursts were corrected for the constant background and analyzed alongside the experimental bursts.

We estimated the 95% confidence intervals in the burst data analyses using statistical bootstrapping. Each experimental set of N bursts was resampled 200 times, with each resampling involving random drawing with replacement, allowing some bursts to be selected multiple times, while others might not be selected at all. For each condition (apo and ligand-bound), we analyzed the re-sampled datasets individually and determined the mean values and 95% confidence intervals for the values determined in each analysis approach.

The variance analysis of the ABEL-FRET data

Our variance analysis builds on the approach of Burst Variance Analysis[73], which we adapted for the analysis of ABEL-FRET data. For each burst, the standard deviation of the bin-wise PRs (σ) was calculated. Bursts were grouped by burst-wise PR in $N = 51$ equally spaced intervals (PR_i, PR_{i+1}) with centers at PR = 0.00, 0.02, 0.04, … 0.98, 1.00. Only groups with >20 bursts were analyzed. Within each group, the mean value of σ ($<\sigma>$) was determined and plotted against the PR values in the centers of the intervals $0.5*(PR_i + PR_{i+1})$. The analysis was performed for the experimental data and the simulated data for the "static heterogeneity" scenario. Statistical bootstrapping was performed to estimate the 95% confidence intervals of $<\sigma>$.

The correlation-based analysis of the ABEL-FRET data

We calculated the correlation functions $G^{AxA}(\tau)$, $G^{DxD}(\tau)$, $G^{DxA}(\tau)$, and $G^{sum\,x\,sum}(\tau)$, for the fluorescence intensities of donor (D), acceptor (A), or their sum, all measured in 1-ms time-bins (all after donor excitation):

$$G^{X\times Y}(\tau) = \frac{\langle X_k(t)\cdot Y_k(t+\tau)\rangle_{t,k}}{\langle X_k(t)\rangle_{t,k}\cdot\langle Y_k(t+\tau)\rangle_{t,k}} - 1 \tag{4a}$$

with $X_k(t)$ and $Y_k(t+\tau)$ the fluorescence intensities of correlated channels X and Y in the k-th burst at times t and $t+\tau$ from the start of that burst. The averaging, denoted with angle brackets, was performed as follows:

$$G^{X\times Y}(\tau) = \frac{\left(\sum_{k:T_k>\tau}\sum_{t=0}^{T_k-\tau-1}X_k(t)Y_k(t+\tau)\right)\cdot\left(\sum_{k:T_k>\tau}(T_k-\tau)\right)}{\left(\sum_{k:T_k>\tau}\sum_{t=0}^{T_k-\tau-1}X_k(t)\right)\cdot\left(\sum_{k:T_k>\tau}\sum_{t=0}^{T_k-\tau-1}Y_k(t+\tau)\right)} - 1 \tag{4b}$$

The burst width is denoted as T_k. Statistical bootstrapping was performed to estimate the 95% confidence intervals of $G^{X\times Y}(\tau)$.

We also calculated the autocorrelation function $g^{PR\times PR}(\tau)$ for the PR values measured in 1-ms time-bins. To compare the correlation curves between the experimental data and the simulated data for the "static heterogeneity" and "static homogeneity" scenarios, we normalized the autocorrelation functions with the standard deviations of PR:

$$g^{PR\times PR}(\tau) = \frac{\langle \delta PR_k(t)\cdot\delta PR_k(t+\tau)\rangle_{t,k}}{\sigma_{PR}^{(t)}\cdot\sigma_{PR}^{(t+\tau)}} \tag{5}$$

$\delta PR_k(t)$ and $\delta PR_k(t+\tau)$ are the deviations of the PR in the k-th burst at times t and $t+\tau$ from the start of that burst from their ensemble-averaged mean values:

$$\mu^{(t)} = \frac{\sum_{k:T_k>\tau}\sum_{t=0}^{T_k-\tau-1}PR_k(t)}{\sum_{k:T_k>\tau}T_k-\tau}\,;\ \mu^{(t+\tau)} = \frac{\sum_{k:T_k>\tau}\sum_{t=0}^{T_k-\tau-1}PR_k(t+\tau)}{\sum_{k:T_k>\tau}T_k-\tau} \tag{6ab}$$

The standard deviations are calculated as:

$$\sigma_{PR}^{(t)} = \left(\frac{\sum_{k:T_k>\tau}\sum_{t=0}^{T_k-\tau-1}\left(PR_k(t)-\mu^{(t)}\right)^2}{\sum_{k:T_k>\tau}T_k-\tau}\right)^{1/2};$$
$$\sigma_{PR}^{(t+\tau)} = \left(\frac{\sum_{k:T_k>\tau}\sum_{t=0}^{T_k-\tau-1}\left(PR_k(t+\tau)-\mu^{(t+\tau)}\right)^2}{\sum_{k:T_k>\tau}T_k-\tau}\right)^{1/2} \tag{7ab}$$

The numerator in Eq. 5 is calculated as:

$$\left\langle \delta \mathrm{PR}_k(t) \cdot \delta \mathrm{PR}_k(t+\tau) \right\rangle_{t,k} = \frac{\sum_{k:T_k>\tau} \sum_{t=0}^{T_k-\tau-1} \left(\left(\mathrm{PR}_k(t) - \mu^{(t)} \right) \cdot \left(\mathrm{PR}_k(t+\tau) - \mu^{(t+\tau)} \right) \right)}{\sum_{k:T_k>\tau} T_k - \tau}$$

As a Pearson correlation coefficient for $\mathrm{PR}_k(t)$ and $\mathrm{PR}_k(t+\tau)$, the normalized autocorrelation function $g^{\mathrm{PR}\times\mathrm{PR}}(\tau)$ can have values from -1 to 1, and equals zero if $\mathrm{PR}(t)$ and $\mathrm{PR}(t+\tau)$ are not correlated. $g^{\mathrm{PR}\times\mathrm{PR}}(\tau)$ functions were calculated for the experimental data and for the simulated data for the "static heterogeneity" and "static homogeneity" scenarios. Statistical bootstrapping was performed to estimate the 95% confidence intervals of $g^{\mathrm{PR}\times\mathrm{PR}}(\tau)$.

The recurrence analysis of PR distributions

Our Recurrence Analysis builds on the approach of Recurrence Analysis of Single Particles[108], which we adapted for the analysis of the ABEL-FRET data. For each burst dataset, PR values were calculated in 1-ms time-bins. Here, $\mathrm{PR}_i(t)$ represents the PR value in the i-th burst at time t from the start of that burst. $\widetilde{\mathrm{PR}}$ denotes the median value of the $\mathrm{PR}_i(t)$ across all time-bins in all bursts. The time-bins, where $\mathrm{PR}_i(t) > \widetilde{\mathrm{PR}}$ were named "high FRET" regions (HF), and time-bins with $\mathrm{PR}_i(t) < \widetilde{\mathrm{PR}}$ were named "low FRET" regions (LF).

For the time-lags $\tau = 1$ ms and $\tau = 200$ ms, we histogrammed the values $\mathrm{PR}_i(t)$ across all bursts longer than τ ($i : \omega_i > \tau$) and all time-points t, where both t-τ and t are within the burst edges (t: $0 \le t-\tau, t \le \omega_i$) and $\mathrm{PR}_i(t\text{-}\tau)$ belongs either to the LF-region (Start at LF: $PR_i(t-\tau) < \widetilde{PR}$) or to the HF-region (Start at HF: $PR_i(t-\tau) > \widetilde{PR}$). For reference, we also histogrammed the $\mathrm{PR}_i(t)$ values across all bursts and all time-points.

Further, for various time-lags τ, we calculated the conditional probabilities of observing $\mathrm{PR}_i(t)$ in the HF region ($\mathrm{PR}_i(t) > \widetilde{\mathrm{PR}}$), given that $\mathrm{PR}_i(t-\tau)$ belonged to either the LF region (Start at LF: $\mathrm{PR}_i(t-\tau) < \widetilde{\mathrm{PR}}$) or to HF region (Start at HF: $\mathrm{PR}_i(t-\tau) > \widetilde{\mathrm{PR}}$). These two probabilities were plotted as functions of τ.

$$\text{Start at HF} : p(\mathrm{HF}(t)|\mathrm{HF}(t-\tau)) = p\left(\mathrm{PR}_i(t) > \widetilde{\mathrm{PR}} | \mathrm{PR}_i(t-\tau) > \widetilde{\mathrm{PR}}; i : \omega_i \ge \tau; t : 0 \le t-\tau, t \le \omega_i \right) \quad (8)$$

$$\text{Start at LF} : p(\mathrm{HF}(t)|\mathrm{LF}(t-\tau)) = p\left(\mathrm{PR}_i(t) > \widetilde{\mathrm{PR}} | \mathrm{PR}_i(t-\tau) < \mathrm{PR}; i : \omega_i \ge \tau; t : 0 \le t-\tau, t \le \omega_i \right) \quad (9)$$

The analysis was performed for the experimental data and for the simulated data in the "Static heterogeneity" scenario. Statistical bootstrapping was performed to estimate the 95% confidence intervals of $p(\mathrm{HF}(t)|\mathrm{HF}(t-\tau))$ and $p(\mathrm{HF}(t)|\mathrm{LF}(t-\tau))$.

Data availability

All data supporting this study's findings are available upon request from the corresponding author(s). The burst data from ABEL-FRET experiments are available in Zenodo with the identifier https://doi.org/10.5281/zenodo.16091079.

Code availability

Marking of the fluorescence bursts was performed in the "Burst Analyzer" software (Becker & Hickl). Further analysis was performed via custom Python scripts available in Zenodo with the identifier https://doi.org/10.5281/zenodo.16091079.

Received: 6 August 2025; Accepted: 4 February 2026;
Published online: 09 March 2026

References

1. Kristiansen, K. Molecular mechanisms of ligand binding, signaling, and regulation within the superfamily of G-protein-coupled receptors: molecular modeling and mutagenesis approaches to receptor structure and function. *Pharmacol. Ther.* **103**, 21–80 (2004).
2. Gether, U. Uncovering molecular mechanisms involved in activation of G protein-coupled receptors. *Endocr. Rev.* **21**, 90–113 (2000).
3. Fredriksson, R., Lagerström, M. C., Lundin, L.-G. & Schiöth, H. B. The G-protein-coupled receptors in the human genome form five main families. phylogenetic analysis, paralogon groups, and fingerprints. *Mol. Pharmacol.* **63**, 1256–1272 (2003).
4. Hauser, A. S., Attwood, M. M., Rask-Andersen, M., Schiöth, H. B. & Gloriam, D. E. Trends in GPCR drug discovery: new agents, targets and indications. *Nat. Rev. Drug Discov.* **16**, 829–842 (2017).
5. Wootten, D., Christopoulos, A., Marti-Solano, M., Babu, M. M. & Sexton, P. M. Mechanisms of signalling and biased agonism in G protein-coupled receptors. *Nat. Rev. Mol. Cell Biol.* **19**, 638–653 (2018).
6. Katritch, V., Cherezov, V. & Stevens, R. C. Structure-function of the G protein-coupled receptor superfamily. *Annu. Rev. Pharmacol. Toxicol.* **53**, 531–556 (2013).
7. Latorraca, N. R., Venkatakrishnan, A. J. & Dror, R. O. GPCR dynamics: structures in motion. *Chem. Rev.* **117**, 139–155 (2016).
8. Gusach, A. et al. Beyond structure: emerging approaches to study GPCR dynamics. *Curr. Opin. Struct. Biol.* **63**, 18–25 (2020).
9. Hilger, D. The role of structural dynamics in GPCR-mediated signaling. *FEBS J.* **288**, 2461–2489 (2021).
10. Kenakin, T. Theoretical aspects of GPCR-ligand complex pharmacology. *Chem. Rev.* **117**, 4–20 (2017).
11. Thal, D. M., Glukhova, A., Sexton, P. M. & Christopoulos, A. Structural insights into G-protein-coupled receptor allostery. *Nature* **559**, 45–53 (2018).
12. Wootten, D., Christopoulos, A. & Sexton, P. M. Emerging paradigms in GPCR allostery: implications for drug discovery. *Nat. Rev. Drug Discov.* **12**, 630–644 (2013).
13. Smith, J. S., Lefkowitz, R. J. & Rajagopal, S. Biased signalling: from simple switches to allosteric microprocessors. *Nat. Rev. Drug Discov.* **17**, 243–260 (2018).
14. Gurevich, V. V. & Gurevich, E. V. Biased GPCR signaling: possible mechanisms and inherent limitations. *Pharmacol. Ther.* **211**, 107540 (2020).
15. García-Nafría, J. & Tate, C. G. Structure determination of GPCRs: cryo-EM compared with X-ray crystallography. *Biochem. Soc. Trans.* **49**, 2345–2355 (2021).
16. Congreve, M., de Graaf, C., Swain, N. A. & Tate, C. G. Impact of GPCR structures on drug discovery. *Cell* **181**, 81–91 (2020).
17. Casiraghi, M. Biophysical investigations of class A GPCRs. *Biochimie* **205**, 86–94 (2022).
18. Prosser, R. S. & Alonzi, N. A. Discerning conformational dynamics and binding kinetics of GPCRs by 19F NMR. *Curr. Opin. Pharmacol.* **72**, 102377 (2023).
19. Agyemang, E., Gonneville, A. N., Tiruvadi-Krishnan, S. & Lamichhane, R. Exploring GPCR conformational dynamics using single-molecule fluorescence. *Methods* **226**, 35–48 (2024).
20. Quast, R. B. & Margeat, E. Studying GPCR conformational dynamics by single molecule fluorescence. *Mol. Cell. Endocrinol.* **493**, 110469 (2019).
21. Ploetz, E. et al. A new twist on PIFE: photoisomerisation-related fluorescence enhancement. *Methods Appl. Fluoresc.* **12**, 012001 (2023).
22. Doose, S., Neuweiler, H. & Sauer, M. Fluorescence quenching by photoinduced electron transfer: a reporter for conformational dynamics of macromolecules. *ChemPhysChem* **10**, 1389–1398 (2009).

23. Dimura, M. et al. Quantitative FRET studies and integrative modeling unravel the structure and dynamics of biomolecular systems. *Curr. Opin. Struct. Biol.* **40**, 163–185 (2016).
24. Lerner, E. et al. FRET-based dynamic structural biology: challenges, perspectives and an appeal for open-science practices. *eLife* **10**, e60416 (2021).
25. Lamichhane, R., Solem, A., Black, W. & Rueda, D. Single-molecule FRET of protein-nucleic acid and protein-protein complexes: surface passivation and immobilization. *Methods* **52**, 192–200 (2010).
26. Kümmerlin, M., Mazumder, A. & Kapanidis, A. N. Bleaching-resistant, near-continuous single-molecule fluorescence and FRET based on fluorogenic and transient DNA binding. *ChemPhysChem* **24**, e202300175 (2023).
27. Elenko, M. P., Szostak, J. W. & van Oijen, A. M. Single-molecule binding experiments on long time scales. *Rev. Sci. Instrum.* **81**, 083705 (2010).
28. Vermeer, B. & Schmid, S. Can DyeCycling break the photobleaching limit in single-molecule FRET? *Nano Res.* **15**, 9818–9830 (2022).
29. Friedel, M., Baumketner, A. & Shea, J.-E. Effects of surface tethering on protein folding mechanisms. *Proc. Natl. Acad. Sci. USA* **103**, 8396–8401 (2006).
30. Talaga, D. S. et al. Dynamics and folding of single two-stranded coiled-coil peptides studied by fluorescent energy transfer confocal microscopy. *Proc. Natl. Acad. Sci. USA* **97**, 13021–13026 (2000).
31. Gilboa, B. et al. Confinement-free wide-field ratiometric tracking of single fluorescent molecules. *Biophys. J.* **117**, 2141–2153 (2019).
32. Yuan, H., Xia, T., Schuler, B. & Orrit, M. Temperature-cycle single-molecule FRET microscopy on polyprolines. *Phys. Chem. Chem. Phys.* **13**, 1762–1769 (2011).
33. Santoso, Y. & Kapanidis, A. N. Probing biomolecular structures and dynamics of single molecules using in-gel alternating-laser excitation. *Anal. Chem.* **81**, 9561–9570 (2009).
34. Kim, J.-Y., Kim, C. & Lee, N. K. Real-time submillisecond single-molecule FRET dynamics of freely diffusing molecules with liposome tethering. *Nat. Commun.* **6**, 6992 (2015).
35. Tyagi, S. et al. Continuous throughput and long-term observation of single-molecule FRET without immobilization. *Nat. Methods* **11**, 297–300 (2014).
36. Banterle, N. & Lemke, E. A. Nanoscale devices for linkerless long-term single-molecule observation. *Curr. Opin. Biotechnol.* **39**, 105–112 (2016).
37. Enderlein, J. Tracking of fluorescent molecules diffusing within membranes. *Appl. Phys. B* **71**, 773–777 (2000).
38. Mieskes, F., Ploetz, E., Wehnekamp, F., Rat, V. & Lamb, D. C. Multicolor 3D orbital tracking. *Small* **19**, e2204726 (2023).
39. Keller, A. M. et al. Multicolor three-dimensional tracking for single-molecule fluorescence resonance energy transfer measurements. *Anal. Chem.* **90**, 6109–6115 (2018).
40. Fields, A. P. & Cohen, A. E. Electrokinetic trapping at the one nanometer limit. *Proc. Natl. Acad. Sci. USA* **108**, 8937–8942 (2011).
41. Wang, Q., Goldsmith, R. H., Jiang, Y., Bockenhauer, S. D. & Moerner, W. E. Probing single biomolecules in solution using the anti-brownian electrokinetic (ABEL) trap. *Acc. Chem. Res.* **45**, 1955–1964 (2012).
42. Wilson, H. & Wang, Q. ABEL-FRET: tether-free single-molecule FRET with hydrodynamic profiling. *Nat. Methods* **18**, 816–820 (2021).
43. Cohen, A. E. & Moerner, W. E. Method for trapping and manipulating nanoscale objects in solution. *Appl. Phys. Lett.* **86**, 093109 (2005).
44. Wang, Q. & Moerner, W. E. Optimal strategy for trapping single fluorescent molecules in solution using the ABEL trap. *Appl. Phys. B Lasers Opt.* **99**, 23–30 (2010).
45. Chu, J. et al. Single-molecule fluorescence multiplexing by multi-parameter spectroscopic detection of nanostructured FRET labels. *Nat. Nanotechnol.* **19**, 1150–1157 (2024).
46. Bockenhauer, S., Fürstenberg, A., Yao, X. J., Kobilka, B. K. & Moerner, W. E. Conformational dynamics of single G protein-coupled receptors in solution. *J. Phys. Chem. B* **115**, 13328–13338 (2011).
47. Dathe, A. et al. Observing monomer: dimer transitions of neurotensin receptors 1 in single SMALPs by homoFRET and in an ABELtrap. *Proc. SPIE* **10884**, 108840N (2019).
48. Jacobson, K. A. & Gao, Z. G. Adenosine receptors as therapeutic targets. *Nat. Rev. Drug Discov.* **5**, 247–264 (2006).
49. Vincenzi, F. et al. Pharmacology of adenosine receptors: recent advancements. *Biomolecules* **13**, 1387 (2023).
50. Jacobson, K. A., Tosh, D. K., Jain, S. & Gao, Z. G. Historical and current adenosine receptor agonists in preclinical and clinical development. *Front. Cell. Neurosci.* **13**, 1–17 (2019).
51. Jacobson, K. A., Suresh, R. R. & Oliva, P. A2A adenosine receptor agonists, antagonists, inverse agonists and partial agonists. *Int. Rev. Neurobiol.* **170**, 1–27 (2023).
52. Zhang, K., Wu, H., Hoppe, N., Manglik, A. & Cheng, Y. Fusion protein strategies for cryo-EM study of G protein-coupled receptors. *Nat. Commun.* **13**, 4366 (2022).
53. García-Nafría, J., Lee, Y., Bai, X., Carpenter, B. & Tate, C. G. Cryo-EM structure of the adenosine A2A receptor coupled to an engineered heterotrimeric G protein. *eLife* **7**, e35946 (2018).
54. Martynowycz, M. W. et al. A robust approach for MicroED sample preparation of lipidic cubic phase embedded membrane protein crystals. *Nat. Commun.* **14**, 1086 (2023).
55. Martynowycz, M. W. et al. MicroED structure of the human adenosine receptor determined from a single nanocrystal in LCP. *Proc. Natl. Acad. Sci. USA* **118**, e2106041118 (2021).
56. Doré, A. S. et al. Structure of the adenosine A(2A) receptor in complex with ZM241385 and the xanthines XAC and caffeine. *Structure* **19**, 1283–1293 (2011).
57. Jaakola, V.-P. et al. The 2.6 angstrom crystal structure of a human A2A adenosine receptor bound to an antagonist. *Science* **322**, 1211–1217 (2008).
58. Xu, F. et al. Structure of an agonist-bound human A2A adenosine receptor. *Science* **332**, 322–327 (2011).
59. Lebon, G. et al. Agonist-bound adenosine A2A receptor structures reveal common features of GPCR activation. *Nature* **474**, 521–525 (2011).
60. Carpenter, B., Nehmé, R., Warne, T., Leslie, A. G. W. & Tate, C. G. Structure of the adenosine A2A receptor bound to an engineered G protein. *Nature* **536**, 104–107 (2016).
61. Clark, L. D. et al. Ligand modulation of sidechain dynamics in a wild-type human GPCR. *eLife* **6**, e28505 (2017).
62. Eddy, M. T. et al. Allosteric coupling of drug binding and intracellular signaling in the A2A adenosine receptor. *Cell* **172**, 68–80.e12 (2018).
63. Eddy, M. T. et al. Extrinsic tryptophans as NMR probes of allosteric coupling in membrane proteins: application to the A2A adenosine receptor. *J. Am. Chem. Soc.* **140**, 8228–8235 (2018).
64. Ye, L., Van Eps, N., Zimmer, M., Ernst, O. P. & Prosser, R. S. Activation of the A2A adenosine G-protein-coupled receptor by conformational selection. *Nature* **533**, 265–268 (2016).
65. Mizumura, T. et al. Activation of adenosine A2A receptor by lipids from docosahexaenoic acid revealed by NMR. *Sci. Adv.* **6**, eaay8544 (2020).
66. Sušac, L., Eddy, M. T., Didenko, T., Stevens, R. C. & Wüthrich, K. A2A adenosine receptor functional states characterized by 19F-NMR. *Proc. Natl. Acad. Sci. USA* **115**, 12733–12738 (2018).
67. Fernandes, D. D. et al. Ligand modulation of the conformational dynamics of the A2A adenosine receptor revealed by single-molecule fluorescence. *Sci. Rep.* **11**, 5910 (2021).
68. Maslov, I. et al. Sub-millisecond conformational dynamics of the A2A adenosine receptor revealed by single-molecule FRET. *Commun. Biol.* **6**, 362 (2023).

69. Wei, S. et al. Slow conformational dynamics of the human A2A adenosine receptor are temporally ordered. *Structure* **30**, 329–337.e5 (2022).
70. Wei, S. et al. Single-molecule visualization of human A2A adenosine receptor activation by a G protein and constitutively activating mutations. *Commun. Biol.* **6**, 1218 (2023).
71. Ballesteros, J. A. & Weinstein, H. Integrated methods for the construction of three-dimensional models and computational probing of structure-function relations in G protein-coupled receptors. *Methods Neurosci.* **25**, 366–428 (1995).
72. Luginina, A. et al. Functional GPCR expression in eukaryotic LEXSY system. *J. Mol. Biol.* **435**, 168310 (2023).
73. Torella, J. P., Holden, S. J., Santoso, Y., Hohlbein, J. & Kapanidis, A. N. Identifying molecular dynamics in single-molecule FRET experiments with burst variance analysis. *Biophys. J.* **100**, 1568–1577 (2011).
74. Kubatova, N., Schmidt, T., Wang, Q. & Clore, G. M. Dimerization propensity of the β1-adrenergic receptor in lipid nanodiscs probed by DEER and single-molecule spectroscopies. *Proc. Natl. Acad. Sci. USA* **122**, e2519609122 (2025).
75. Heitkamp, T. & Börsch, M. Fast ATP-dependent subunit rotation in reconstituted FoF1-ATP synthase trapped in solution. *J. Phys. Chem. B* **125**, 7638–7650 (2021).
76. Su, B. et al. Observing conformations of single FoF1-ATP synthases in a fast anti-Brownian electrokinetic trap. *Proc. SPIE* **9329**, 93290A (2015).
77. Pérez, I., Heitkamp, T. & Börsch, M. Mechanism of ADP-inhibited ATP hydrolysis in single proton-pumping FoF1-ATP synthase trapped in solution. *Int. J. Mol. Sci.* **24**, 8442 (2023).
78. Schlau-Cohen, G. S., Wang, Q., Southall, J., Cogdell, R. J. & Moerner, W. E. Single-molecule spectroscopy reveals photosynthetic LH2 complexes switch between emissive states. *Proc. Natl. Acad. Sci. USA* **110**, 10899–10903 (2013).
79. Denisov, I. G. & Sligar, S. G. Nanodiscs for the study of membrane proteins. *Curr. Opin. Struct. Biol.* **87**, 102844 (2024).
80. Denisov, I. G. & Sligar, S. G. Nanodiscs in membrane biochemistry and biophysics. *Chem. Rev.* **117**, 4669–4713 (2017).
81. Gulezian, E. et al. Membrane protein production and formulation for drug discovery. *Trends Pharmacol. Sci.* **42**, 657–674 (2021).
82. Pettersen, J. M., McCracken, O. & Robinson, A. S. Ligand binding kinetics to evaluate the function and stability of A2AR in nanodiscs. *Biophys. J.* **124**, 440–457 (2025).
83. Bocquet, N. et al. Real-time monitoring of binding events on a thermostabilized human A2A receptor embedded in a lipid bilayer by surface plasmon resonance. *Biochim. Biophys. Acta* **1848**, 1224–1233 (2015).
84. Eddy, M. T., Martin, B. T. & Wüthrich, K. A2A Adenosine receptor partial agonism related to structural rearrangements in an activation microswitch. *Structure* **29**, 170–176.e3 (2021).
85. Huang, S. K. et al. Delineating the conformational landscape of the adenosine A receptor during G protein coupling. *Cell* **184**, 1884–1894.e14 (2021).
86. Thakur, N. et al. Anionic phospholipids control mechanisms of GPCR-G protein recognition. *Nat. Commun.* **14**, 794 (2023).
87. Kalinin, S., Sisamakis, E., Magennis, S. W., Felekyan, S. & Seidel, C. A. M. On the origin of broadening of single-molecule FRET efficiency distributions beyond shot noise limits. *J. Phys. Chem. B* **114**, 6197–6206 (2010).
88. Wang, Q. & Moerner, W. E. Lifetime and spectrally resolved characterization of the photodynamics of single fluorophores in solution using the anti-Brownian electrokinetic trap. *J. Phys. Chem. B* **117**, 4641–4648 (2013).
89. Du, Y. et al. Assembly of a GPCR-G protein complex. *Cell* **177**, 1232–1242.e11 (2019).
90. Diez, M. et al. Proton-powered subunit rotation in single membrane-bound F0F1-ATP synthase. *Nat. Struct. Mol. Biol.* **11**, 135–141 (2004).
91. Zimmermann, B., Diez, M., Zarrabi, N., Gräber, P. & Börsch, M. Movements of the epsilon-subunit during catalysis and activation in single membrane-bound H(+)-ATP synthase. *EMBO J.* **24**, 2053–2063 (2005).
92. Düser, M. G., Bi, Y., Zarrabi, N., Dunn, S. D. & Börsch, M. The proton-translocating a subunit of F0F1-ATP synthase is allocated asymmetrically to the peripheral stalk. *J. Biol. Chem.* **283**, 33602–33610 (2008).
93. Sielaff, H., Dienerowitz, F. & Dienerowitz, M. Single-molecule FRET combined with electrokinetic trapping reveals real-time enzyme kinetics of individual F-ATP synthases. *Nanoscale* **14**, 2327–2336 (2022).
94. Squires, A. H., Cohen, A. E. & Moerner, W. E. Anti-Brownian Traps. in *Encyclopedia of Biophysics* 1–8. https://doi.org/10.1007/978-3-642-35943-9_486-1 (Springer, 2018).
95. Fields, A. P. & Cohen, A. E. Anti-Brownian traps for studies on single molecules. *Methods Enzymol.* **475**, 149–174 (2010).
96. Carpenter, W. B., Lavania, A. A., Squires, A. H. & Moerner, W. E. Label-free anti-brownian trapping of single nanoparticles in solution. *J. Phys. Chem. C. Nanomater. Interfaces* **128**, 20275–20286 (2024).
97. Cohen, A. E. & Moerner, W. E. An all-glass microfluidic cell for the ABEL trap: fabrication and modeling. *Proc. SPIE* **5930**, 191–198 (2005).
98. Juette, M. F. et al. The bright future of single-molecule fluorescence imaging. *Curr. Opin. Chem. Biol.* **20**, 103–111 (2014).
99. Isselstein, M. et al. Self-healing dyes—keeping the promise? *J. Phys. Chem. Lett.* **11**, 4462–4480 (2020).
100. Foote, A. K., Ishii, K., Cullinane, B., Tahara, T. & Goldsmith, R. H. Quantifying microsecond solution-phase conformational dynamics of a DNA hairpin at the single-molecule level. *ACS Phys. Chem. Au* **4**, 408–419 (2024).
101. Cullinane, B., Ishii, K., Kaur, S., Tahara, T. & Goldsmith, R. H. Evidence of a three-state mechanism in DNA hairpin folding. *J. Am. Chem. Soc.* **147**, 13101–13107 (2025).
102. Squires, A. H., Wang, Q., Dahlberg, P. D. & Moerner, W. E. A bottom-up perspective on photodynamics and photoprotection in light-harvesting complexes using anti-Brownian trapping. *J. Chem. Phys.* **156**, 070901 (2022).
103. Yang, H.-Y. & Moerner, W. E. Resolving mixtures in solution by single-molecule rotational diffusivity. *Nano Lett.* **18**, 5279–5287 (2018).
104. Rendler, T. et al. Monitoring single membrane protein dynamics in a liposome manipulated in solution by the ABELtrap. *Proc. SPIE* **7902**, 7902M (2011).
105. Zarrabi, N. et al. Asymmetry of rotational catalysis of single membrane-bound F0F1-ATP synthase. *Proc. SPIE* **5699**, 175–188 (2005).
106. Dienerowitz, M., Dienerowitz, F. & Börsch, M. Measuring nanoparticle diffusion in an ABELtrap. *J. Opt.* **20**, 034006 (2018).
107. Pérez, I., Krueger, A., Wrachtrup, J., Jelezko, F. & Börsch, M. Single NV center in nanodiamond for quantum sensing of protein dynamics in an ABEL trap. *Proc. SPIE* **12849**, 1284906 (2024).
108. Hoffmann, A. et al. Quantifying heterogeneity and conformational dynamics from single molecule FRET of diffusing molecules: Recurrence analysis of single particles (RASP). *Phys. Chem. Chem. Phys.* **13**, 1857–1871 (2011).
109. Chung, S. H. & Kennedy, R. A. Forward-backward non-linear filtering technique for extracting small biological signals from noise. *J. Neurosci. Methods* **40**, 71–86 (1991).
110. Efron, B. & Tibshirani, R. J. *An Introduction to the Bootstrap*. https://doi.org/10.1201/9780429246593 (Chapman and Hall/CRC 1994).

Acknowledgements
The authors acknowledge Dr. Polina Khorn (Moscow Institute of Physics and Technology, MIPT), who performed protein expression, labeling, purification, and nanodisc reconstitution under the supervision of Dr. Aleksey Mishin and V.C. I.M. acknowledges BOF UHasselt (BOF21BL11) and funding from the European Union under the HORIZON TMA MSCA Postdoctoral Fellowships action (project MemProDx, 101149735). J.He. acknowledges the Research Foundation Flanders (FWO, grant number G0B9922N). V.B. acknowledges DAAD Young Talents Programme Line A. M.B. gratefully acknowledges ABEL trap funding by the Deutsche Forschungsgemeinschaft (DFG) through grants BO1891/10-2, BO1891/15-1, BO1891/16-1, BO1891/18-2. Additional support for the ABEL trap was provided by an ACP Explore project within the ProExcellence initiative ACP2020 from the State of Thuringia to the Abbe Center of Photonics (Jena).

Author contributions
M.B. prepared the instrumentation for the ABEL-FRET measurements. I.M., M.B., and T.G. collected ABEL-FRET data. I.M. and T.G. performed burst marking under the supervision of M.B. I.M. analyzed the ABEL-FRET data and produced the first draft of the manuscript under the supervision of J.Ho., J.He., V.B., V.C., M.B., and T.G. I.P. performed diffusion analysis under the supervision of M.B. I.M., V.B., M.B., and T.G. conceptualized the study. All the authors contributed to analyzing data, writing the original draft, reviewing, and editing.

Funding
Open Access funding enabled and organized by Projekt DEAL.

Competing interests
The authors declare no competing interests.

Additional information
Supplementary information The online version contains supplementary material available at https://doi.org/10.1038/s42004-026-01941-8.

Correspondence and requests for materials should be addressed to Michael Börsch or Thomas Gensch.

Peer review information *Communications Chemistry* thanks Ryan J. Durham and the other, anonymous, reviewer(s) for their contribution to the peer review of this work.